Journal of Materials Chemistry A

COMMUNICATION

View Article Online
View Journal | View Issue

Cite this: J. Mater. Chem. A, 2015, 3, 10199

Received 17th March 2015
Accepted 2nd April 2015

DOI: 10.1039/c5ta01960e

www.rsc.org/MaterialsA

Highly flexible and transferable supercapacitors with ordered three-dimensional MnO_2/Au/MnO_2 nanospike arrays†

Yuan Gao,[a] Huanyu Jin,[b] Qingfeng Lin,[a] Xiang Li,[a] Mohammad Mahdi Tavakoli,[a] Siu-Fung Leung,[a] Wing Man Tang,[b] Limin Zhou,[c] Helen Lai Wa Chan[b] and Zhiyong Fan*[a]

Ordered three-dimensional nanostructures are highly attractive for energy storage application, particularly for high-performance flexible supercapacitors. Here, we report a unique MnO_2/Au/MnO_2 nanospike (MAMNSP) supercapacitor structure based on free-standing 3-D gold (Au) NSP films. The NSP films are highly flexible and transferable onto an arbitrary flexible substrate to enable applications that require high flexibility. The large surface area of this unique structure leads to a remarkable enhancement in electrochemical performance, 1.9 and 4.26 times higher capacitance as compared with MnO_2/Au NSP (MANSP) and MnO_2/planar (MAPL) electrodes, respectively. The all-solid-state symmetric supercapacitors based on MAMNSP electrodes have been fabricated and systematic performance characterization showed that the devices have a high volumetric capacitance of 20.35 F cm^{-3} and a specific energy of 1.75 $\times$ 10^{-3} W h cm^{-3}. In addition, the bendability measurement showed that the supercapacitor devices are highly flexible and reliable. By virtue of simple fabrication procedures and enhanced electrochemical performance, such 3-D structures have highly promising potential for portable and flexible energy storage systems for a wide range of practical applications.

Introduction

Three-dimensional nanostructures, such as arrays of nanowires (NWs), nanopillars (NPLs), nanospikes (NSPs), nanocones (NCNs), *etc.*, naturally have a large surface/interface area which can be harnessed for applications that are sensitive to surface processes, such as chemical/biological sensing[1,2] and surface catalysis,[3,4] as well as energy generation[5,6] and storage.[7,8] Particularly for energy storage, these nanostructures have been primarily used in supercapacitors and batteries.[9,10] As compared with batteries, supercapacitors have appealing attributes including fast charging–discharging rate, more safe operation and long cycle life-time, thus they have triggered enormous research interest.[11–14] It is worth noting that due to the fast growth of the portable electronics market, reliable, light weight and flexible energy storage devices are in urgent demand. Therefore, extensive research has been carried out on nanostructure based flexible supercapacitors.[15–25] In fact, in most of the existing studies, the nanostructures have relatively thick supporting substrates, or the structures themselves have a thickness of tens of micrometers to millimeters. Thus their bendability/flexibility has a constraint.[16,26,27] Herein, we report a unique supercapacitor structure based on ultra-thin, free-standing 3-D gold (Au) NSP films. The NSP films are highly flexible and transferable onto an arbitrary flexible substrate to enable applications that require high flexibility. The large surface area of NSPs is utilized to achieve respectable pseudo-capacitance together with a thin layer of MnO_2 coating. The all-solid-state symmetric supercapacitors based on MnO_2/Au/MnO_2 NSP (MAMNSP) electrodes have been fabricated in this work and systematic performance characterization showed that the devices have a volumetric capacitance of 20.35 F cm^{-3} and the highest specific energy and specific power of 1.75 $\times$ 10^{-3} W h cm^{-3} and 13.46 W cm^{-3}, respectively. Furthermore, the bendability measurement showed that the supercapacitor devices are highly flexible and reliable. They are operational even at a bending angle of 180° and they can preserve 88% capacitance after 5000 cycles of bending. These results have shown that the flexible

[a]Department of Electronic and Computer Engineering, Hong Kong University of Science and Technology, Clear Water Bay, Kowloon, Hong Kong SAR, China. E-mail: eezfan@ust.hk

[b]Department of Applied Physics, The Hong Kong Polytechnic University, Hung Hom, Hong Kong SAR, China

[c]Department of Mechanical Engineering, The Hong Kong Polytechnic University, Hung Hom, Hong Kong SAR, China

† Electronic supplementary information (ESI) available: Photographs of the mechanical robustness test of the Au NSP film and the schematic illustration of point contacts among NSPs are shown in Fig. S1. Optical image of the free-standing Au NSP film and Si stamps with the area of 1.5 cm × 1.5 cm are shown in Fig. S2. SEM images of Au NSPs with the pitches of 0.5 μm, 1 μm, 1.2 μm and 1.5 μm are shown in Fig. S3. Schematic illustration of surface area calculation and surface enhancement results are shown in Fig. S4. XPS and XRD of the materials are shown in Fig. S5. SEM images at different electrodeposition times are shown in Fig. S6. CV curves after different electrodeposition times (5–120 s) and related areal capacitance are shown in Fig. S7. CV (300–500 mV s^{-1}) and GCD (0.3–5 mA cm^{-2}) curves of the MAMNSP electrode after an electrodeposition time of 45 s are shown in Fig. S8. See DOI: 10.1039/c5ta01960e

NSP electrodes are highly promising for use in high performance and flexible supercapacitor devices.

Results and discussion

The free-standing Au NSP film fabrication process mainly comprises six steps shown in Fig. 1: (i) nanoimprint assisted electrochemical preparation of a template with aluminum (Al) NSPs (Fig. 1a and b). This process was previously developed by us for nanostructured solar cells;[5] (ii) wet etching of anodized aluminum oxide to achieve pure Al NSPs (Fig. 1c); (iii) low voltage anodization on the Al NSP substrates to achieve a thin sacrificial layer of alumina (light blue colored layer in Fig. 1d) on NSPs; (iv) sputtering of a 100 nm and highly conductive Au layer on alumina NSPs (Fig. 1e); (v) etching away the sacrificial alumina layer and transfer of the Au NSP film onto an arbitrary flexible substrate; (vi) re-anodization of the patterned substrate to form NSPs again. It is worth pointing out that in this fabrication scheme, the substrate is reusable for many cycles and only one time nanoimprint is required, thus greatly reducing the process cost and complexity.

Fig. 2a shows a photograph of the Au NSP film transferred onto a piece of regular Xerox printing paper demonstrating its appealing flexibility, and the inset scanning electron microscopy (SEM) image shows the microstructure of a free-standing NSP electrode upon bending. Interestingly, it is discovered in our work that the NSP electrode film is quite robust. As shown in the ESI (Fig. S1†), the film can be directly picked up from an aqueous solution with tweezers. Upon leaving the surface of the solution, the film wraps itself to form a roll due to water surface tension. And when the roll of the film is placed back to the solution, the film unwraps itself naturally without any observable wrinkles and cracks. Unlike 2-D films that consist of metal nanowire networks, which need a packaging material to maintain their robustness,[28] this interesting behavior of the unique structure can be rationalized by considering: (i) the relative inert surface of Au itself, (ii) the excellent flexibility of the 100 nm Au film and most importantly (iii) the fact that the NSP structure leads to point contact between the NSPs and the backside of the

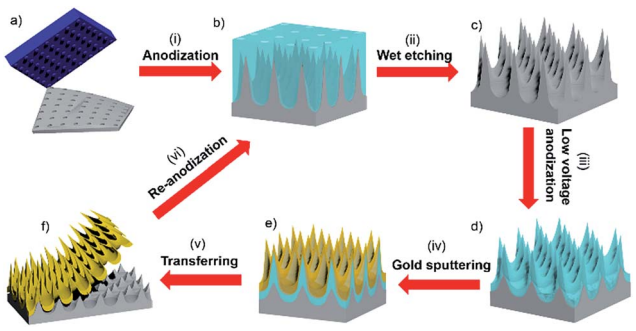

Fig. 1 Schematic illustration showing the fabrication process of the free-standing Au NSP film. (a) Nanoimprint process with an ordered square nanopillar Si mold. (b) Aluminum oxide achieved by anodization. (c) As-prepared Al NSP template. (d) Alumina NSPs achieved by low voltage anodization. (e) 100 nm Au-coated alumina NSPs. (f) Free-standing Au NSP film after etching away the sacrificial alumina layer.

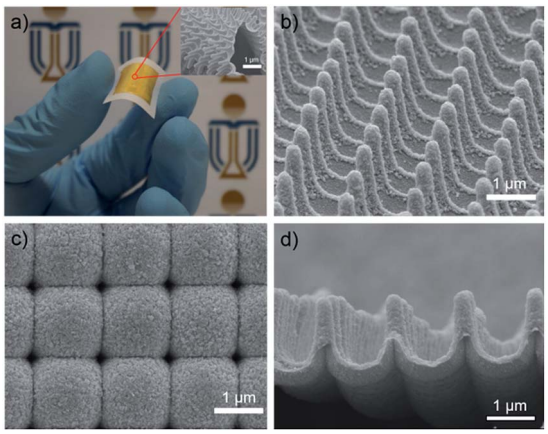

Fig. 2 (a) Photographs of the free-standing Au NSP film transferred onto a regular Xerox printing paper and the SEM image (insert) shows the microstructure upon bending. (b–d) SEM images of the as-prepared MAMNSP electrode, (b) top view, (c) back view and (d) side view.

Au film when it forms a roll, thus leading to a much lower binding energy in the roll, as schematically shown in ESI Fig. S1g.† The excellent flexibility and transferability render the Au NSP film compatible with various types of substrates. Besides the paper substrates shown in Fig. 2a, the polycarbonate (PC) plastic substrate can also serve as the holding substrate for the Au NSP film (ESI, Fig. S2a†).

In the past, we have discovered that the geometric factors of the NSPs, including pitch and height can be precisely engineered.[5,29] For photovoltaic applications, there exists an intermediate and optimal aspect ratio that arose from the balanced design considering both optical light trapping and the uniformity of photovoltaic thin film deposition. While for applications such as supercapacitors, a naturally large surface area is preferred. To obtain an optimized structure with the highest surface area, Au NSP films with different pitches, including 0.5 μm, 1 μm, 1.2 μm, and 1.5 μm, were fabricated (ESI, Fig. S3a–d†). It was measured that the heights of NSP arrays according to these pitches are 0.42 μm, 0.98 μm, 1.22 μm, and 1.57 μm, respectively. In order to identify the structure with the largest surface area, surface area calculation was performed using the structural schematics (ESI, Fig. S4a†). As a result, it was found that NSPs with the pitches of 1 μm, 1.2 μm, and 1.5 μm have a fairly close surface area which is nearly 3.3 times that of the area of a flat planar electrode with the same projected area (ESI, Fig. S4b†). Considering the fact that a larger pitch is preferable for more uniform Au film sputtering, 1.5 μm pitch NSP films were chosen for the subsequent device fabrication, and such films can be fabricated as large as 1.5 cm × 1.5 cm with excellent uniformity (ESI, Fig. S2b†).

Flexible and transferable Au NSP films are preferable structures for flexible supercapacitor devices, due to their enlarged surface area. In order to realize a NSP based supercapacitor device, MnO_2 was electrochemically deposited onto the Au NSP film electrode. Since the Xerox paper has certain porosity, MnO_2 was eventually deposited onto both the front side and the back

side of the Au NSP film forming the MAMNSP configuration. This unique feature leads to more efficient utilization of the NSP film surface area. Due to the conformal nature of electrodeposition, the NSP shape can be well preserved after electrodeposition of 40 nm MnO_2 layers. Fig. 2b shows the tilted angle view SEM of the front side of a MnO_2 coated NSP array with the conformity clearly demonstrated. Fig. 2c shows the dome-like structure at the back side of the NSP film and the cavities at the corners of the domes can be resolved. These cavities are the result of etching of the alumina NSPs (Fig. 1c), and they provide an additional large surface area at the back side of NSPs as well. Meanwhile, a nanoflake structure can be observed on the MnO_2 surface and this nanoflake structure could further increase the electrode surface area and promote ion diffusion and expedite electron transfer. The cross-sectional SEM image of the MAMNSP electrode is shown in Fig. 2d, the height of NSPs is 1.5 μm and the thickness of the MnO_2 nanoflake film is around 40 nm on each side. The detailed chemical composition of the MAMNSP electrode was probed by X-ray photoelectron spectroscopy (XPS) (ESI, Fig. S5a and b†), two peaks at 641.9 eV and 653.7 eV can be identified, which indicates that the Mn^{4+} ions are dominant in the product. Wide angle X-ray diffraction results of the as-prepared MAMNSP electrode are also shown in Fig. S5c.†

To evaluate the electrochemical performance of the MAMNSP electrode, cyclic voltammetry (CV) measurements of a three-electrode configuration based on the as-prepared electrode with a 0.5 cm × 0.5 cm footprint area were conducted in 1 M Na_2SO_4 liquid electrolyte with voltage ranging from 0 to 0.8 V. Fig. 3a presents the typical CV curves at a scan rate of 100 mV s^{-1} after electrodeposition of MnO_2 on different structures including MAMNSPs, MnO_2/Au NSPs (MANSPs), and MnO_2/Au planar (MAPL). Note that the MANSP structure refers to the non-transferred Au film deposited on alumina NSPs thus only the front side of the NSP film was deposited with a layer of the MnO_2 film, and the MAPL structure is a planar glass sputtered with 100 nm thick Au. In addition, MnO_2 mass loading on these three structures are the same for the sake of a fair comparison. It can be seen from Fig. 3a that a much more symmetrically rectangular shape and a larger area surrounded by the CV curve shows that the MAMNSP electrode has the best pseudo-capacitive behavior. Galvanostatic charge–discharge (GCD) characteristics based on different architectures are also plotted in Fig. 3b. Notably, the lower voltage drop of 0.011 V for MAMNSPs suggests lower internal resistance, which is the result of thinner MnO_2 in the MAMNSP structure since it has the largest area among all three structures with the same MnO_2 mass loading. And the larger area enclosed by the charge–discharge curves demonstrates that more charge is stored in the electrode by the complete redox reaction of the active material on the surface, which can also be attributed to the larger surface area of the electrode with thinner mass loading. The areal capacitance and the specific capacitance are two critical parameters to determine the pseudo-capacitive performance of an electrode, which can be calculated by using the following equations:

$$C_s = \int_0^{0.8} \left(\left|I_{Au/MnO_2}\right| - \left|I_{Au}\right|\right) dU / 2m\Delta U v_0 \quad (1)$$

$$C_a = \int_0^{0.8} \left(\left|I_{Au/MnO_2}\right| - \left|I_{Au}\right|\right) dU / 2s\Delta U v_0 \quad (2)$$

$$m = QM/2eN_A \quad (3)$$

where C_s and C_a are the specific capacitance and the areal capacitance of the electrode, respectively. m and s are the mass of MnO_2 and the footprint area of the electrode. I is the electric current, U is the voltage, ΔU is the operating voltage window (0.8 V), and v_0 is the scan rate. Q is the amount of charge passing through the entire electrode, M is the molecular weight of MnO_2, e is the electron charge, and N_A is Avogadro's number. As shown in Fig. 3c, the areal capacitance for MAMNSPs, MANSPs, and MAPL at a scan rate of 10 mV s^{-1} is 17.44 mF cm^{-2}, 9.01 mF cm^{-2}, and 4.09 mF cm^{-2}, respectively. Overall, the MAMNSP electrode shows 1.9 times higher capacitance than that of MANSPs. Meanwhile, the capacitance of the MAMNSP electrode is 4.26 times that of the MAPL electrode, which is a logical result of the double side conformal electrodeposition of MnO_2. With the same mass loading, such superior performance can only be ascribed to the enhanced surface area of the NSP electrodes, and the larger surface area for the same mass loading leads to a thinner layer of MnO_2 coating on NSPs, which can potentially shorten the distance for both electron and ion diffusion, leading to better faradic surface charge storage. To further confirm this hypothesis, electrodeposition of MnO_2 at different times (5 s to 120 s) was conducted on free-standing Au NSPs, as shown in Fig. S6.† The CV performance of the MAMNSP electrode shows that an electrodeposition time of 45 s is necessary to achieve the best performance (ESI, Fig. S7a and b†). Therefore, 45 s deposition time was used for all MAMNSP electrodes and that led to a 40 nm thick MnO_2 layer on NSPs.

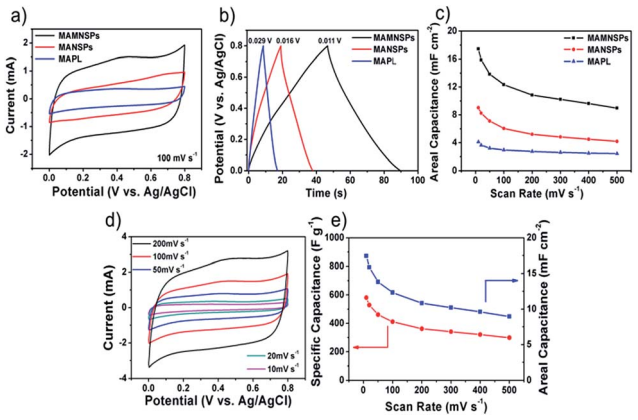

Fig. 3 (a) CV curves of MAMNSP, MANSP and MAPL electrodes at a scan rate of 100 mV s^{-1} in 1 M aqueous Na_2SO_4 electrolyte. (b) GCD curves of MAMNSP, MANSP and MAPL electrodes at the same current density (0.3 mA cm^{-2}) with different voltage drops. (c) Areal capacitance of MAMNSP, MANSP, MAPL electrodes as a function of the scan rate. (d) CV curves of the MAMNSP electrode at different scan rates (10 mV s^{-1} to 200 mV s^{-1}). (e) Areal and specific capacitance of MAMNSPs at different scan rates.

This result clearly indicates that excessive thickness of MnO_2 hinders ion and charge transport which in turn compromises the overall electrochemical capacitance and this is consistent with a previous report.[15] Meanwhile, Fig. 3d and ESI Fig. S8a† show CV curves of a MAMNSP electrode at different scan rates after 45 s electrodeposition. Obviously, these CV curves still retain a symmetrically rectangular shape without any distortion with increasing scan rate from 10 mV s^{-1} to 500 mV s^{-1}, demonstrating a highly reversible redox reaction. GCD curves with different current densities (0.3 mA cm^{-2} to 5 mA cm^{-2}) are also plotted in ESI Fig. S8b.† The highly symmetric curve for the charge and discharge process indicates the excellent capacitive behavior of the MAMNSP electrode. According to Fig. 3e, the specific and areal capacitance are 581.3 F g^{-1} and 17.44 mF cm^{-2} at a scan rate of 10 mV s^{-1} and 298.6 F g^{-1} and 8.96 mF cm^{-2} at a scan rate of 500 mV s^{-1}. The excellent rate capability further demonstrates the advantages of the as-fabricated electrode.

To further explore the practical merit of the MAMNSP electrodes, an all-solid-state symmetric supercapacitor was fabricated using the following process. Two pieces of Au NSP films were transferred onto two pieces of regular Xerox printing paper followed by electrodeposition of MnO_2 to achieve MAMNSP electrodes. Thereafter, they were uniformly coated with H_3PO_4/poly(vinyl alcohol) (PVA) gel electrolyte and assembled together. The all-solid-state device was finally achieved by drying up the excess water in the gel electrolyte. The electrochemical performance of the device was evaluated by CV measurements at a scan rate from 10 mV s^{-1} to 200 mV s^{-1} as shown in Fig. 4a. GCD curves with different current densities from 0.2 mA cm^{-2} to 2 mA cm^{-2} were also plotted in Fig. 4b. Note that the nice rectangular shape of the CV curve and linear voltage–time profiles achieved from the GCD curve demonstrate a good capacitive performance. As shown in Fig. 4c, the areal capacitance and volumetric capacitance for the device is 8.14 mF cm^{-2} and 20.35 F cm^{-3} at a current density of 0.2 mA cm^{-2}. Since the volumetric capacitance and energy density are size-dependent, we have successfully decreased the volume of the device. The SEM cross section image of the device is inserted in Fig. 4c, it is composed of two pieces of as-prepared electrodes (1.5 μm for each) and the gel electrolyte, and the total thickness of the device is as thin as 4 μm without taking into account the thickness of the paper substrate. The specific energy and specific power based on the volume of the device were calculated according to the following formula:

$$E = C_V(\Delta E)^2/2 \quad (4)$$

$$P = (\Delta E)^2/4RV \quad (5)$$

$$R = U_{drop}/2I \quad (6)$$

$$C_V = I/(-dU/dt) \quad (7)$$

where E and P are the specific energy and the specific power calculated based on the volume. C_V is the volumetric capacitance of the device, ΔE is the operating voltage window excluding the voltage drop (U_{drop}), R is the internal resistance of the device, V is the volume of the device, I is the constant discharge current, and dU/dt is the slope of the discharge curve. The Ragone plot shows the specific energy with respect to the specific power calculated based on the volume of the device, as can be seen in Fig. 4d. The highest specific energy of the as-fabricated device is 1.75×10^{-3} W h cm^{-3} at a specific power of 12.01 W cm^{-3}, which is among the highest when compared with the previously reported values.[30–35]

To further test the electrochemical performance of the device, electrochemical impedance spectroscopy (EIS) measurements were conducted in the frequency range of 100 kHz to 0.01 Hz and the results are shown in Fig. 5a. Equivalent series resistance (ESR) as low as 11 Ω can be obtained at the x intercept of the Nyquist plot. The small radius of the semicircle in the high frequency range reflects the small charge-transfer resistance and the straight line nearly parallel to the imaginary axis at low frequency demonstrates the ideal capacitive behavior.[36] For practical operation of a flexible supercapacitor device, bending performance and cyclic stability are two important characteristics.[37–42] In this regard, CV measurements when a device is folded and released were conducted at a scan rate of 100 mV s^{-1}. As shown in Fig. 5b, there is no apparent change in the CV curve and the calculated capacitance difference is only 1.3% after being released. Fig. 5c shows the capacitance at different bending angles (0°, 45°, 90°, 135°, and 180°), confirming the marginal performance change with bending of the device. Fig. 5d shows the capacitance retention after multiple cycles of the CV scan at a rate of 100 mV s^{-1} within the voltage test window of 0 to 0.8 V. It can be seen that the capacitance still maintains nearly 94% of its initial value after 1000 cycles and 88% after 5000 cycles, which shows excellent cycle life.

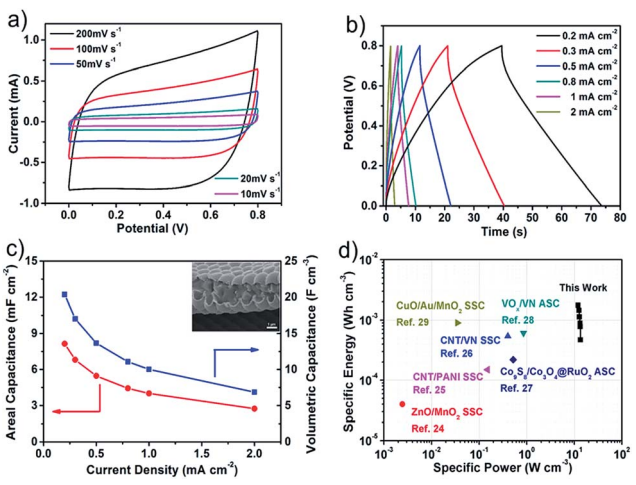

Fig. 4 (a) CV curves of the symmetric supercapacitor at different scan rates (10 mV s^{-1} to 200 mV s^{-1}). (b) GCD curves of the supercapacitor device with different current densities (0.2 mA cm^{-2} to 2 mA cm^{-2}). (c) Areal capacitance and volumetric capacitance of the device as a function of different discharge current densities and SEM (insert) shows that the device thickness is around 4 μm. (d) Ragone plot shows the specific energy and specific power of the device.

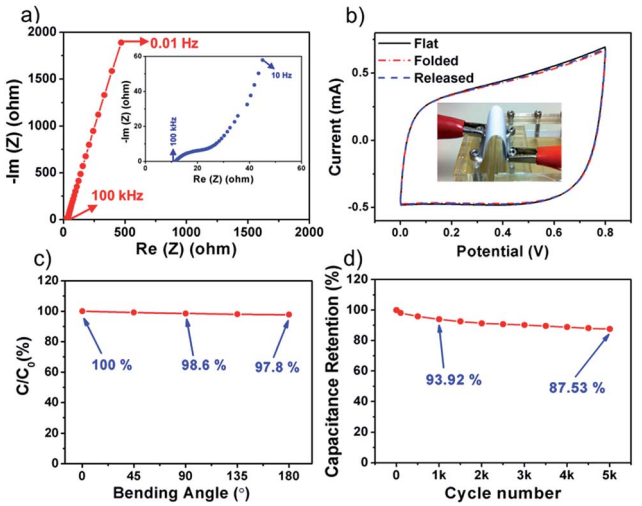

Fig. 5 (a) Nyquist plot of the symmetric supercapacitor device. (b) CV measurements at a scan rate of 100 mV s^{-1} when the device is folded and released. (c) Device bending test at different angles. (d) Cycling performance of the device during 5000 cycles at a scan rate of 100 mV s^{-1}.

Conclusions

Herein, we report ordered freestanding 3-D MAMNSP electrodes fabricated on 3-D Au NSP architecture. The ultra-thin Au NSP films have excellent transferability and flexibility. The large surface area of this unique structure leads to a remarkable enhancement in the electrochemical performance, 1.9 and 4.26 times higher capacitance as compared with MANSP and MAPL electrodes, respectively. Moreover, the all-solid-state symmetric supercapacitors based on MAMNSP electrodes fabricated in this work showed that the devices have a high volumetric capacitance of 20.35 F cm^{-3} and a specific energy of 1.75×10^{-3} W h cm^{-3}. In addition, the marginal change of the capacitance upon bending measurement and the attractive cyclic stability showed that the supercapacitor devices are highly flexible and reliable. By virtue of simple fabrication procedures and enhanced electrochemical performance, such 3-D structures have highly promising potential for portable and flexible energy storage systems for a wide range of practical applications.

Experimental section

Preparation of the aluminum NSP template

Aluminum foil with a thickness of 0.25 mm and an area of 3 cm × 2 cm was prepared by cutting, followed by electrochemical cleaning under a constant voltage of 15 V for 2 min. After that, 1.5 cm × 1.5 cm silicon stamps with ordered square nanopillars with a height of 0.2 μm and controllable pitches including 0.5 μm, 1 μm, 1.2 μm, and 1.5 μm were utilized as imprinting molds to produce a nanoindentation array on the surface of the as-prepared aluminum foil. Afterwards, the aluminum NSP template with different pitches was achieved by one-step anodization and wet etching processes with proper control of the solution concentration, temperature, time and direct current (DC) voltage.

Fabrication of the freestanding Au NSPs film

Aluminum NSPs with a 1.5 μm pitch was first converted into alumina NSPs *via* a low voltage anodization process (20 V in 3.4 wt% H_2SO_4 for 16 h), for use as the etching layer. Thereafter, 100 nm Au was uniformly coated onto alumina NSPs by sputtering deposition, followed by etching the template in an acidic solution composed of 1.8 wt% H_2CrO_4 and 6 wt% H_3PO_4 at a temperature of 70 °C for 5 h. The etching solution was then neutralized with DI water after the Au NSP film detached from the template and floated. Arbitrary substrates such as Xerox printing paper, PC, *etc.* could be immersed into solution and placed below the film. Ultimately, the as-fabricated film could lie on the target substrates after draining away the solution with a syringe pump.

Fabrication of MAMNSP electrodes

The Au NSP film was transferred onto Xerox paper followed by an anode deposition process. Different amounts of MnO_2 were deposited by precisely controlling the time from 5 s to 120 s with a constant current density of 0.25 mA cm^{-2} at room temperature. The deposition solution consists of 0.01 M manganese acetate ($MnAc_2$), 98% purity and 0.02 M ammonium acetate (NH_4Ac), 99% purity dissolved in 90% DI water and 10% dimethyl sulfoxide (DMSO).

Assembling of all-solid-state symmetric supercapacitors

12 g PVA and 12 g 85 wt% H_3PO_4 were dissolved in 120 mL DI water. After that, the solution was vigorously stirred at 85 °C until it became clear. Then, the solution was cooled down to room temperature and used as a gel electrolyte. Two pieces of MAMNSP electrodes were fabricated beforehand, and one of the as-proposed electrodes was immersed into H_3PO_4/poly(vinyl alcohol) (PVA) gel electrolyte for 5 min. Due to the porous nature of the Xerox printing paper, the gel electrolyte could penetrate through the substrate and thus the electrode could be coated on both sides with the gel electrolyte. Afterwards, to achieve uniform distribution of the gel electrolyte, spin coating was performed at the rotation speed of 4000 rpm for 2 min. Thereafter, the as-proposed electrode was placed onto a hotplate at a temperature of 60 °C for 1 h to vaporize the excess water. A similar way but without the drying process was used for the other MAMNSP electrode, and after spin coating, the electrode was directly placed onto the previous one to finish assembling the final device.

Characterization of samples

Various analytical techniques were utilized to characterize the as-built nanostructured electrodes. Morphologies were characterized using field-emission scanning electron microscopy (JSM-7100F, Japan). Chemical compositions were studied by X-ray photoelectron spectroscopy (PHI 5600, USA). CV, GCD and EIS measurements based on both two-electrode and three-

electrode configurations were performed on an electrochemical workstation (CHI 660E, China). CV was carried out at different scan rates of 10, 20, 50, 100, 200 and 500 mV s^{-1}. GCD was measured at 0.2, 0.3, 0.5, 0.8, 1, 2, and 5 mA cm^{-2}. EIS was measured in the frequency range of 100 kHz to 0.01 Hz with a potential amplitude of 10 mV.

Acknowledgements

This work was supported by the General Research Fund (612113) from the Hong Kong Research Grant Council and partially supported by the Hong Kong Innovation and Technology Fund (ITS/117/13) from the Innovation and Technology Commission. The authors also thank Dr S. Y. Gan from the Chang Chun Institute of Applied Chemistry, the Chinese Academy of Sciences for his helpful discussion.

Notes and references

1 K. Skucha, Z. Y. Fan, K. Jeon, A. Javey and B. Boser, *Sens. Actuators, B*, 2010, **145**, 232–238.
2 Z. Y. Fan and J. G. Lu, *Appl. Phys. Lett.*, 2005, **86**, 123510.
3 J. Li, Y. Qiu, Z. Wei, Q. Lin, Q. Zhang, K. Yan, H. Chen, S. Xiao, Z. Fan and S. Yang, *Energy Environ. Sci.*, 2014, **7**, 3651–3658.
4 Y. Qiu, S. Leung, Q. Zhang, B. Hua, Q. Lin, Z. Wei, K. Tsui, Y. Zhang, S. Yang and Z. Fan, *Nano Lett.*, 2014, **14**, 2123–2139.
5 S. Leung, L. Gu, Q. Zhang, K. Tsui, J. Shieh, C. Shen, T. Hsiao, C. Hsu, L. Lu, D. Li, Q. Lin and Z. Fan, *Sci. Rep.*, 2014, **4**, 4243.
6 Q. Lin, S. Leung, L. Lu, X. Chen, Z. Chen, H. Tang, W. Su, D. Li and Z. Fan, *ACS Nano*, 2014, **8**, 6484–6490.
7 Y. Qiu, Y. Zhao, X. Yang, W. Li, Z. Wei, J. Xiao, S. Leung, Q. Lin, H. Wu and Y. Zhang, *Nanoscale*, 2014, **6**, 3626–3631.
8 Z. Yu, B. Duong, D. Abbitt and J. Thomas, *Adv. Mater.*, 2013, **25**, 3302–3306.
9 D. N. Futaba, K. Hata, T. Yamada, T. Hiraoka, Y. Hayamizu, Y. Kakudate, O. Tanaike, H. Hatori, M. Yumura and S. Iijima, *Nat. Mater.*, 2006, **5**, 987–994.
10 C. K. Chan, H. L. Peng, G. Liu, K. McIlwrath, X. F. Zhang, R. A. Huggins and Y. Cui, *Nat. Nanotechnol.*, 2008, **3**, 31–35, DOI: 10.1038/nnano.2007.411 ER.
11 Y. Gogotsi, *Nature*, 2014, **509**, 568–570.
12 J. R. Miller and P. Simon, *Science Magazine*, 2008, **321**, 651–652.
13 D. Pech, M. Brunet, H. Durou, P. Huang, V. Mochalin, Y. Gogotsi, P. Taberna and P. Simon, *Nat. Nanotechnol.*, 2010, **5**, 651–654.
14 P. Simon and Y. Gogotsi, *Nat. Mater.*, 2008, **7**, 845–854.
15 S. Chabi, C. Peng, D. Hu and Y. Zhu, *Adv. Mater.*, 2014, **26**, 2440–2445.
16 Z. Su, C. Yang, B. Xie, Z. Lin, Z. Zhang, J. Liu, B. Li, F. Kang and C. Wong, *Energy Environ. Sci.*, 2014, **7**, 2652–2659.
17 B. Duong, Z. Yu, P. Gangopadhyay, S. Seraphin, N. Peyghambarian and J. Thomas, *Adv. Mater. Interfaces*, 2014, **1**, DOI: 10.1002/admi.201300014.
18 U. N. Maiti, J. Lim, K. E. Lee, W. J. Lee and S. O. Kim, *Adv. Mater.*, 2014, **26**, 615–619.
19 Z. Yu, C. Li, D. Abbitt and J. Thomas, *J. Mater. Chem. A*, 2014, **2**, 10923–10929.
20 Z. Yu, L. Tetard, L. Zhai and J. Thomas, *Energy Environ. Sci.*, 2015, **8**, 702–730.
21 H. Zhao, C. Wang, R. Vellacheri, M. Zhou, Y. Xu, Q. Fu, M. Wu, F. Grote and Y. Lei, *Adv. Mater.*, 2014, **26**, 7654–7659.
22 R. Yi, S. Chen, J. Song, M. L. Gordin, A. Manivannan and D. Wang, *Adv. Funct. Mater.*, 2014, **24**, 7433–7439.
23 X. Wang, X. Lu, B. Liu, D. Chen, Y. Tong and G. Shen, *Adv. Mater.*, 2014, **26**, 4763–4782.
24 X. Xia, D. Chao, Z. Fan, C. Guan, X. Cao, H. Zhang and H. J. Fan, *Nano Lett.*, 2014, **14**, 1651–1658.
25 X. Xia, Y. Zhang, Z. Fan, D. Chao, Q. Xiong, J. Tu, H. Zhang and H. J. Fan, *Adv. Energy Mater.*, 2014, **5**, DOI: 10.1002/aenm.201401709.
26 M. F. El-Kady, V. Strong, S. Dubin and R. B. Kaner, *Science*, 2012, **335**, 1326–1330, DOI: 10.1126/science.1216744.
27 Z. Su, C. Yang, C. Xu, H. Wu, Z. Zhang, T. Liu, C. Zhang, Q. Yang, B. Li and F. Kang, *J. Mater. Chem. A*, 2013, **1**, 12432–12440.
28 S. Zhu, Y. Gao, B. Hu, J. Li, J. Su, Z. Fan and J. Zhou, *Nanotechnology*, 2013, **24**, 335202.
29 S. Leung, K. Tsui, Q. Lin, H. Huang, L. Lu, J. Shieh, C. Shen, C. Hsu, Q. Zhang and D. Li, *Energy Environ. Sci.*, 2014, **7**, 3611–3616.
30 X. Lu, M. Yu, T. Zhai, G. Wang, S. Xie, T. Liu, C. Liang, Y. Tong and Y. Li, *Nano Lett.*, 2013, **13**, 2628–2633.
31 X. Xiao, X. Peng, H. Jin, T. Li, C. Zhang, B. Gao, B. Hu, K. Huo and J. Zhou, *Adv. Mater.*, 2013, **25**, 5091–5097.
32 J. Xu, Q. Wang, X. Wang, Q. Xiang, B. Liang, D. Chen and G. Shen, *ACS Nano*, 2013, **7**, 5453–5462.
33 P. Yang, X. Xiao, Y. Li, Y. Ding, P. Qiang, X. Tan, W. Mai, Z. Lin, W. Wu and T. Li, *ACS Nano*, 2013, **7**, 2617–2626.
34 M. Yu, Y. Zhang, Y. Zeng, M. Balogun, K. Mai, Z. Zhang, X. Lu and Y. Tong, *Adv. Mater.*, 2014, **26**, 4724–4729.
35 Z. Yu and J. Thomas, *Adv. Mater.*, 2014, **26**, 4279–4285.
36 W. Chen, R. Rakhi, L. Hu, X. Xie, Y. Cui and H. Alshareef, *Nano Lett.*, 2011, **11**, 5165–5172.
37 X. Xiao, T. Li, P. Yang, Y. Gao, H. Jin, W. Ni, W. Zhan, X. Zhang, Y. Cao and J. Zhong, *ACS Nano*, 2012, **6**, 9200–9206.
38 L. Yuan, X. Lu, X. Xiao, T. Zhai, J. Dai, F. Zhang, B. Hu, X. Wang, L. Gong and J. Chen, *ACS Nano*, 2011, **6**, 656–661.
39 L. Chen, Z. Yu, J. Wang, Q. Li, Z. Tan, Y. Zhu and S. Yu, *Nano Energy*, 2015, **11**, 119–128.
40 L. Huang, C. Li and G. Shi, *J. Mater. Chem. A*, 2014, **2**, 968–974.
41 L. Wu, R. Li, J. Guo, C. Zhou, W. Zhang, C. Wang, Y. Huang, Y. Li and J. Liu, *AIP Adv.*, 2013, **3**, 082129.
42 C. Meng, C. Liu, L. Chen, C. Hu and S. Fan, *Nano Lett.*, 2010, **10**, 4025–4031.

